---

**Article:**
Lee, S. orcid.org/0000-0002-5669-1555, Jin, X. orcid.org/0000-0002-7205-3318, Jung, H. et al. (10 more authors) (2023) High gain, low noise 1550 nm GaAsSb/AlGaAsSb avalanche photodiodes. Optica, 10 (2). 147. ISSN 2334-2536

https://doi.org/10.1364/optica.476963

---

Research Article Vol. 10, No. 2 / February 2023 / Optica 147

OPTICA

# High gain, low noise 1550 nm GaAsSb/AlGaAsSb avalanche photodiodes

S. Lee,[1,†] X. Jin,[2,†] H. Jung,[1,†] H. Lewis,[2] Y. Liu,[2] B. Guo,[3] S. H. Kodati,[1] M. Schwartz,[1] C. Grein,[4] T. J. Ronningen,[1] J. P. R. David,[2] Joe. C. Campbell,[3] and S. Krishna[1,*]

[1]Department of Electrical and Computer Engineering, The Ohio State University, Columbus, Ohio 43210, USA
[2]Department of Electronic and Electrical Engineering, University of Sheffield, Sheffield S1 3JD, UK
[3]Department of Electrical and Computer Engineering, University of Virginia, Charlottesville, Virginia 22904, USA
[4]Department of Physics, University of Illinois, Chicago, Illinois 60607, USA
*Corresponding author: krishna.53@osu.edu

Received 29 September 2022; revised 27 November 2022; accepted 6 December 2022; published 24 January 2023

**High sensitivity avalanche photodiodes (APDs) operating at eye-safe infrared wavelengths (1400–1650 nm) are essential components in many communications and sensing systems. We report the demonstration of a room temperature, ultrahigh gain ($M = 278$, $\lambda = 1550$ nm, $V = 69.5$ V, $T = 296$ K) linear mode APD on an InP substrate using a $GaAs_{0.5}Sb_{0.5}/Al_{0.85}Ga_{0.15}As_{0.56}Sb_{0.44}$ separate absorption, charge, and multiplication (SACM) heterostructure. This represents ∼10× gain improvement ($M = 278$) over commercial, state-of-the-art InGaAs/InP-based APDs ($M \sim 30$) operating at 1550 nm. The excess noise factor is extremely low ($F < 3$) at $M = 70$, which is even lower than Si APDs. This design gives a quantum efficiency of 5935.3% at maximum gain. This SACM APD also shows an extremely low temperature breakdown sensitivity ($C_{bd}$) of ∼11.83 mV/K, which is ∼10× lower than equivalent InGaAs/InP commercial APDs. These major improvements in APD performance are likely to lead to their wide adoption in many photon-starved applications.**



https://doi.org/10.1364/OPTICA.476963

## 1. INTRODUCTION

There is significant interest in lidar systems for applications ranging from space-borne instruments for greenhouse gas emission [1,2] to accurate 3D sensing [2] and mapping [2] in urban environments for next-generation fully autonomous vehicles. For these photon-starved applications, avalanche photodiodes (APD) can provide high detection sensitivity due to their internal gain ($M$). However, this gain often comes at the cost of excess noise due to the stochastic nature of the impact ionization process. McIntyre's local field theory [3] defines the excess noise factor ($F$) as

$$F = kM + (1 - k)\,(2 - 1/M)\,,$$

where $k = \beta/\alpha$ (the ratio of impact ionization coefficient of the hole, $\beta$, and electron, $\alpha$). This $F$ sets a limit on the maximum useful gain of a given device, meaning that high sensitivity APDs requiring a large signal-to-noise ratio necessitate the use of avalanche materials with a small $k$.

Currently available lidar systems primarily operate at 905 nm using silicon APD receivers due to their high sensitivity, reliability, and low cost. However, the wavelength of these lidar systems is limited by the bandgap of silicon to less than 1100 nm. Recently, there is growing interest in developing longer wavelength lidar systems. The wavelength of 1550 nm is relevant for long distance applications because higher laser powers can be used (being eye-safe), and because it is less affected by the solar background and atmospheric turbulence.

The best commercially available linear mode APDs at 1550 nm consist of an $In_{0.53}Ga_{0.47}As$ (InGaAs) absorber and InP or InAlAs multiplier in a separate absorption, charge, and multiplication (SACM) architecture. These typically exhibit $M$ of 30 and a large $F > 10$ [4,5]. This relatively small gain and large excess noise limit the performance of these APDs.

In this work, we report a significant advancement in the gain and excess noise of a room temperature (RT, $T = 296$ K), 1550 nm APD using a novel $GaAs_{0.5}Sb_{0.5}/Al_{0.85}Ga_{0.15}As_{0.56}Sb_{0.44}$ (GaAsSb/AlGaAsSb) SACM architecture. In this design, the AlGaAsSb multiplier experiences a high electric field (<600 kV/cm) to achieve a large avalanche gain, while the GaAsSb absorber has a low electric field (<200 kV/cm) region to minimize the tunneling leakage current. The grading from the absorber to the multiplier is accomplished by inserting thin AlGaAsSb layers with two different Al compositions between 0% and 85%.

Figure 1 shows the heterostructure design (a), a microscope image of the devices (b), the modeled electric field profile (c), and the band profile of the device (d). The structure builds on recent work on the AlGaAsSb multiplier [6,7] and our new work on the GaAsSb absorber. The structure was grown on semi-insulating InP

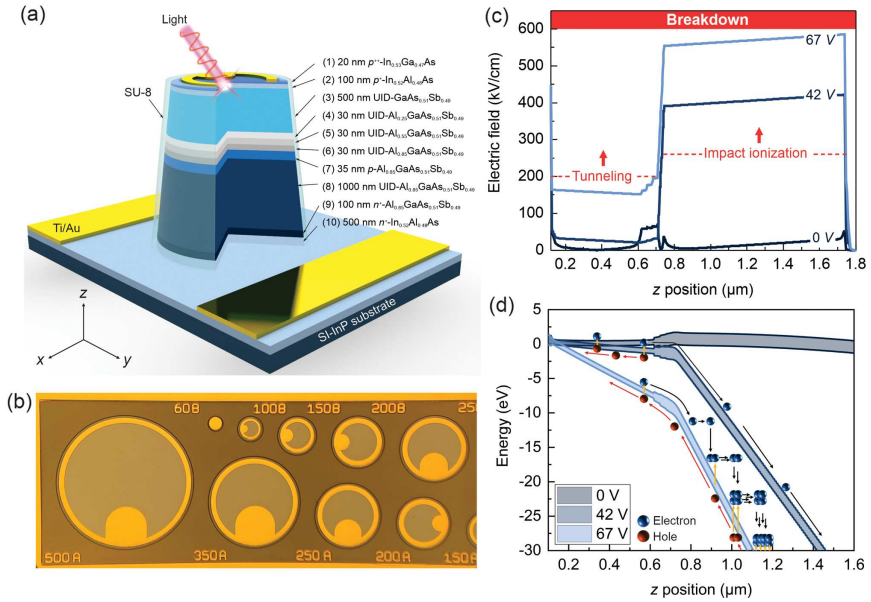


**Fig. 1.** (a) Heterostructure schematic of the GaAsSb/AlGaAsSb SACM APD grown by solid source molecular beam epitaxy. (b) Microscope image of the fabricated devices. Numbers indicate the diameters of the devices in μm. (c) Modeled electric field profile of the structure showing the GaAsSb in the low field region below the tunneling threshold and the AlGaAsSb multiplier in the high field region to obtain large avalanche gain. (d) Band profile for the device at zero bias, punch-through (42 V), and near breakdown voltage (67 V). The graphic shows how the photogenerated carriers travel from the absorber to the multiplier depending on the applied bias voltages. The blue and red circles indicate electrons and holes, respectively.

substrates using solid source molecular beam epitaxy (MBE). More details of the material growth are given in Section 5.

## 2. TESTING OF ABSORBER AND MULTIPLIER FOR GaAsSb/AlGaAsSb SACM APDS

### A. High Performance $GaAs_{0.5}Sb_{0.5}$ Absorber

One of the novelties of this SACM structure is the use of a GaAsSb absorber as opposed to the conventionally used InGaAs. There have been relatively few reports on the use of GaAsSb, lattice-matched to InP, for detector applications [8–10]. For our structure, there were two benefits of using GaAsSb over InGaAs. The first is that the conduction and valence bands in $Al_xGa_{1-x}AsSb$ can be made to change continuously from the GaAsSb absorber to the AlGaAsSb multiplier without any large bandgap discontinuity. This makes it easier to extract the carriers by minimizing trapping and improving the speed of the devices. The second benefit is that it is easier to grade from GaAsSb to AlGaAsSb while maintaining lattice-matched growth, as it is mainly the group III compositions that need to change. By contrast, InGaAs has a type II band alignment, resulting in a larger conduction band offset (∼ 1 eV) between the last layer of grading ($In_{0.52}Al_{0.48}As$) and the AlGaAsSb multiplier [11,12]. Therefore, no comparably simple and efficient grading is possible with an InGaAs absorber.

To examine the performance of the GaAsSb absorber, we grew two $p^+-i-n^+$ structures (PIN1 and PIN2). PIN1 and PIN2 were designed with two different unintentionally doped (UID) layer thicknesses, 1000 and 1800 nm, for measuring the background doping concentration and external quantum efficiency (QE). The details of the structures can be found in Supplement 1. Capacitance–voltage (CV) measurements were performed on PIN1 and PIN2 as shown in Fig. 2(a). From this, the background doping concentrations in the UID layers of PIN1 and PIN2 were found to be as low as $1 \times 10^{15}$ $cm^{-3}$. Figure 2(b) shows the spectra of the measured QE for PIN1 and PIN2. The QEs of PIN1 and PIN2 were 45% and 52.5%, respectively, at 1550 nm without anti-reflection (AR) coating, and the 50% cut-off wavelength was 1675 nm. The absorption coefficient of GaAsSb determined from the measured QE spectra is shown in Fig. 2(c). The absorption spectra of PIN1 and PIN2 are very similar, indicating the high reproducibility of the growth. The absorption coefficients, while broadly similar to those previously reported [7], are slightly higher in the range from 1400 to 1700 nm and are comparable to those of InGaAs [13]. In the SACM APD, the next most important design parameter for the GaAsSb absorber is its tunneling threshold field. We assume the same tunneling threshold field (∼200 kV/cm) as for an InGaAs absorber in designing our SACM APD because of their similar bandgaps and electron-effective masses [14,15] [Fig. 1(c)].

### B. Extremely Low Excess Noise $Al_{0.85}Ga_{0.15}As_{0.56}Sb_{0.44}$ Multiplier

The heart of an APD is the multiplier region. The gain and excess noise of three $p^+-i-n^+$ AlGaAsSb multipliers with varying UID layer thicknesses, 390 (PIN3), 590 (PIN4), and 1020 nm (PIN5), were investigated to support the SACM APD design. This study of the effects of thickness on avalanche characteristics enabled us to select the best thickness for the multiplier in an SACM APD, maximizing $M$ and minimizing the excess noise factor ($F$). Details of the growth and characterization of these structures are given in Supplement 1. All measurements on $M$ and $F$ in this paper were taken using pure electron-initiated multiplication, which was achieved by using short-wavelength light to ensure that > 99% of incident photons were absorbed in the $p$-type cladding regions. Figure 2(d) shows $\log(M-1)$ as a function of reverse bias for PIN3, PIN4, and PIN5. The black dashed lines indicate the theoretical gain curves when $k = 0$ (only electron ionization).

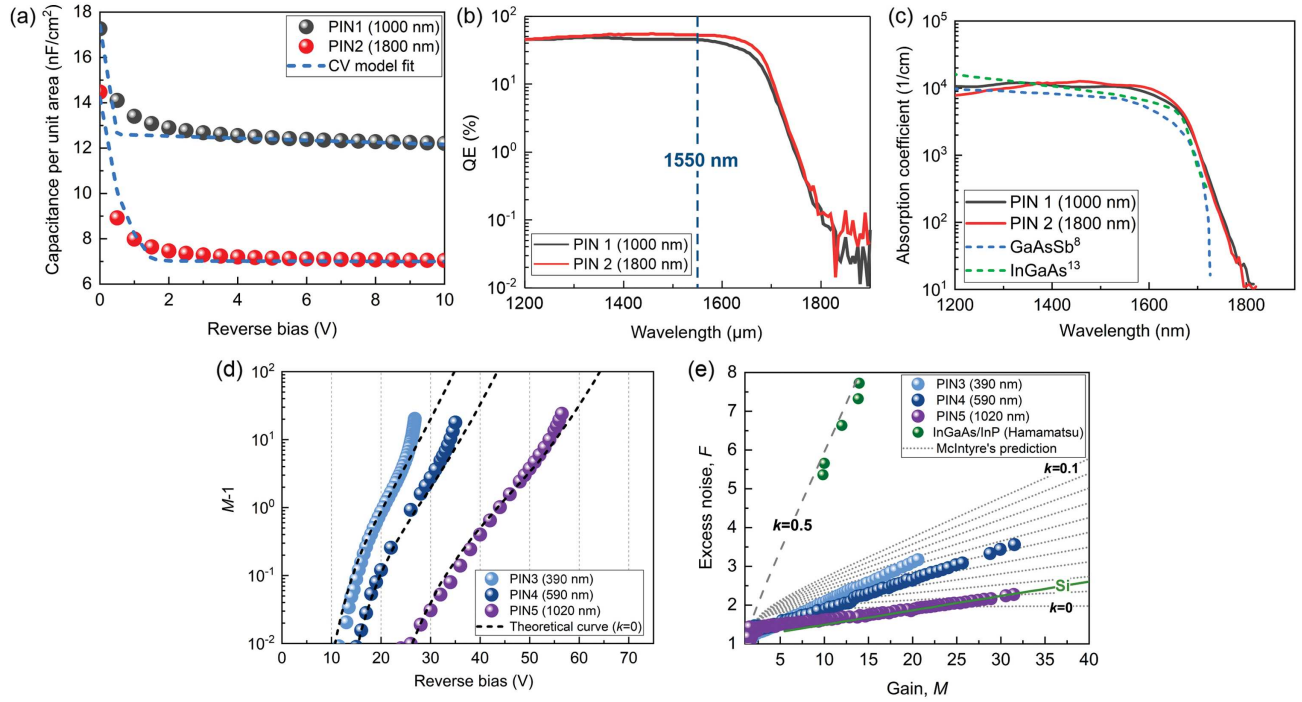


**Fig. 2.** (a) Capacitance–voltage results, (b) external spectral quantum efficiency (without anti-reflection coatings), and (c) absorption coefficients of two GaAsSb PINs (PIN1 and PIN2) compared with literature [8,13]. (d) $M-1$ versus reverse bias and (e) $F$ as a function of $M$ for AlGaAsSb $p^+-i-n^+$ structures with three different multiplier thicknesses. Green dots indicate $F$ of InGaAs/InP Hamamatsu APD [4,5]. Gray dashed lines are the calculated McIntyre's noise curves with different $k$ increasing from 0 to 0.1 in steps of 0.01 and $k = 0.5$.

Interestingly, as the thickness of the multiplier increases, the experimental gain curve approaches that of the theoretical curve, indicating that the thicker the multiplier region, the more closely the device approximates single carrier impact ionization behavior. Figure 2(e) shows $F$ as a function of $M$ for PIN3, PIN4, and PIN5. The lowest $F$ was achieved with the thickest multiplier, PIN5. These results are in good qualitative agreement with the electric field dependence of the ionization coefficients in AlGaAsSb [16]. The thicker multiplier regions operate at lower electric fields where $k$ is smaller, giving lower $F$. However, the measured $F$ for the thickest structure, PIN5, does not follow McIntyre's curve, increasing more slowly with $M$ at low $M$. Previous theoretical work by Ong *et al.* [17] explaining the very low $F$ seen in AlAsSb suggested that the even in thick multiplication regions, non-local and dead space effects can act to reduce $F$. This behavior may therefore be responsible for the $F$ versus $M$ characteristics seen in PIN5. While $F$ may well continue to decrease slightly as the multiplication region width increases, the operating voltage would start to become very large in these structures. Therefore, the optimum avalanche multiplier thickness was chosen to be 1020 nm (PIN5), which provides high gain ($M \sim 30$) at a voltage of ~56 V and has a minimal excess noise factor ($F \sim 2.2$ at $M = 30$). This $F$ value is much lower than obtainable with an InP or even InAlAs multiplier and is similar to a Si APD [18].

## 3. CHARACTERIZATION RESULTS OF GaAsSb/AlGaAsSb SACM APDS

Several iterations of the GaAsSb/AlGaAsSb SACM APDs were grown to optimize the thickness and doping of the grading and charge layers. This study found that a charge layer width of 35 nm with a $p$-type doping of $6 \times 10^{17}$ cm$^{-3}$ ensures the electric fields in the absorber and the multiplier differ as shown in Fig. 1(c).

### A. Results of APD Characterizations

Figure 3(a) shows the measured CV of the GaAsSb/AlGaAsSb SACM APD. Initially, $C$ gradually decreases with reverse bias voltage and then drops again at around 42 V, which indicates the punch-through of the electric field into the absorption layer. To precisely extract the device characteristics, modeling was carried out to fit the experimental CV curve. The actual thicknesses and doping concentrations are slightly different from the designed structure described in Fig. 1(a). The absorber and multiplier thicknesses were found to be 460 and 1100 nm, respectively. Details of the layer thicknesses and doping of the modeled structure can be found in Supplement 1. One interesting observation in the doping profile of the SACM APD [inset of Fig. 3(a)] is that the peak doping concentration of the charge layer is slightly lower than designed, likely due to Be dopant diffusion during material growth. However, including the dopant diffusion, the calculated total doping concentration of the charge layer is almost identical to the designed value of $2.1 \times 10^{12}$ cm$^{-2}$.

The measured dark current for several SACM APDs with differing sizes is shown in Fig. 3(b). The dark current scales with the area more than the perimeter of the devices after punch-through, indicating that the total dark current is mainly limited by carriers crossing the charge barrier, resulting in an increase in the dark current. A small deviation of the punch-through voltage between the simulation and experiment may originate from the variation of the doping concentration or thickness in the charge layer across the wafer. Beyond punch-through, the photocurrent ($I_{ph}$) continues to increase, driven by the avalanche process until it reaches

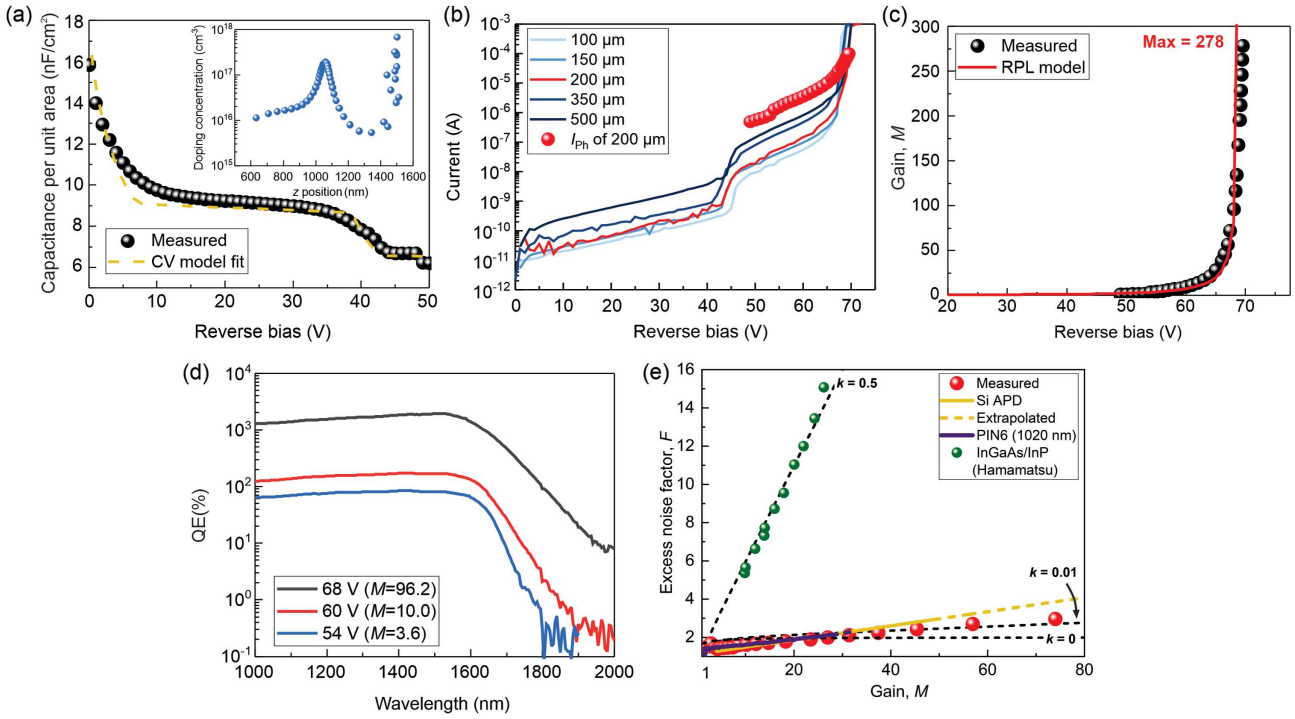


**Fig. 3.** (a) Measured CV result of the SACM APD. The inset shows the calculated doping profile. (b) Bias-dependent dark current for different diode sizes and photocurrent ($I_{ph}$) for 200 μm diameter device at room temperature. Punch-through occurs around 42–45 V, with the photocurrent suddenly increasing by two orders of magnitude higher than the dark current. (c) $M$ obtained with a 1550 nm illumination showing a maximum gain of 278. The random path length (RPL) model fits the measured $M$ curve well. (d) Measured QE spectra of the SACM APD at various reverse bias voltages. (e) Excess noise factor, $F$, as a function of the multiplication gain, $M$. Notice that the commercial infrared multiplier, InP, has very large $F$. The AlGaAsSb layer has an $F$ that is even better than Si.

breakdown around 70 V. There is a slight increase in the photocurrent at 53 V, which is probably due to the grading layers' steps that impede electron transport. This phenomenon can be mitigated by linear grading. Accurate determination of the multiplication as a function of bias requires knowledge of the gain at a particular bias. Since the photocurrent is unreliable below 54 V, all analyses on $M$ and $F$ used data from 54 V onwards. At 54 V, the device is fully depleted, and the electric field in the multiplication region is high enough to give rise to some gain. The $M$ of the SACM APDs was calculated using the electric field distribution obtained from CV modeling [Fig. 3(a)], and the impact ionization coefficients of AlGaAsSb [16], using a random path length (RPL) model [19]. This gave an $M$ of 3.6 at 54 V, which was used to convert the photocurrent shown in Fig. 3(b) into a bias-dependent $M$. The modeled multiplication at voltages $\geq$ 54 V agrees well with the measured photocurrent results as shown in Fig. 3(c).

The maximum measured $M$ was 278, an order of magnitude improvement over commercial 1550 nm APDs. Figure 3(d) shows the measured QE spectra of the SACM APD as a function of wavelength at various reverse biases and hence gains. Comparing the value of the photocurrent at 54 V using 1550 nm in the SACM APD to those in PIN1 and PIN2 at unity gain further corroborated the $M$ value of 3.6.

The QE deduced in the SACM APD at unity gain is relatively low at 21.35% (due primarily to the thin 460 nm GaAsSb layer used) but nevertheless can still achieve 5935.3% (responsivity of 7418 A/W) with gain. One interesting feature in the QE spectra is that the cut-off tail becomes slightly extended to longer wavelengths (~1900 nm) as the applied reverse bias voltage increases, due to the Franz–Keldysh effect [20,21]. This could be useful for other applications such as detection of methane (1650 nm), hydrogen chloride (1742 nm), nitrogen oxide (1814 nm), and water vapor (1854 nm, 1877 nm) [22].

The measured $F$ of the SACM APD structure, shown in Fig. 3(e), does not follow McIntyre's curve, increasing more slowly with $M$ at low $M$ and appears to have the same $F$ versus $M$ characteristic as seen in PIN5 [Fig. 2(e)]. $F$ is approximately 5× lower than that of commercial InP APDs and even lower than that of a low noise commercial Si APD for $M > 25$.

### B. Results of Bandwidth and Temperature Coefficient of Breakdown

The frequency response and the −3 dB bandwidth of the 200 μm devices are shown in Fig. 4(a) and 4(b), respectively. Measurements were undertaken using a CW 1.55 μm semiconductor laser that was modulated by a Mach–Zehnder modulator (MZM) driven by a vector network analyzer (VNA). Further details are provided in Section 5. We focus on 200 μm devices because commercial APD technology for lidar systems typically requires a large optical window to enhance the input signal. The bandwidth gradually increases from 0.2 GHz ($M \sim 8$), saturates at ~ 0.7 GHz ($M \sim 25$), and then starts dropping ($M \sim 100$) due to the avalanche build-up time. With 65 V reverse bias, the highest −3 dB bandwidth and gain–bandwidth product (GBP) were determined to be 0.7 and 11 GHz, respectively. This bandwidth value is comparable to commercial InP-based APDs (~ 0.9 GHz) [5] with a similar diameter and capacitance. The bandwidths of these SACM APDs increase with reducing device diameter, which

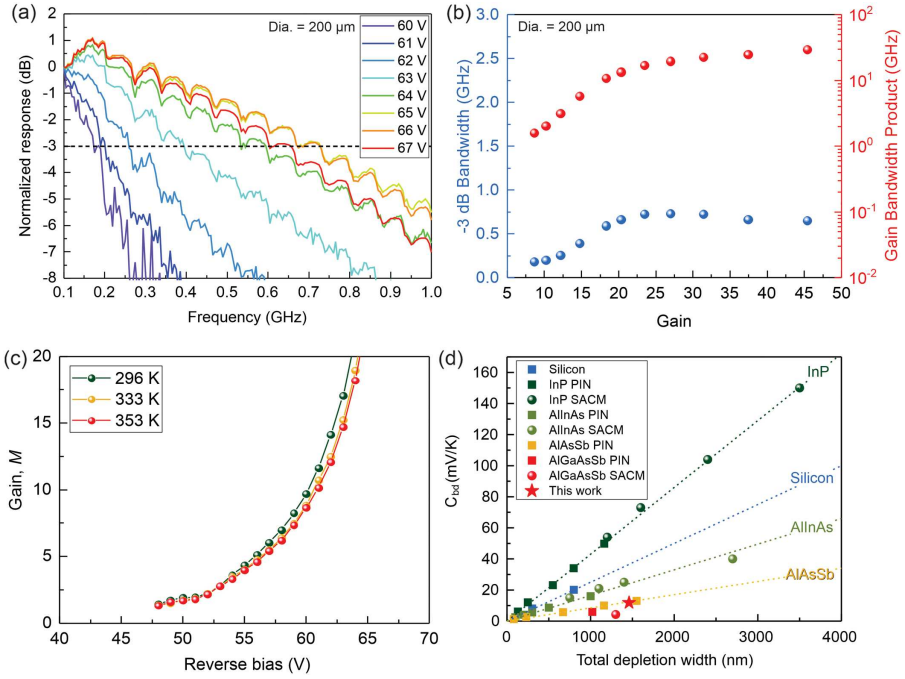


**Fig. 4.** (a) Frequency of GaAsSb/AlGaAsSb APDs as a function of the operating bias measured using a vector network analyzer (VNA) method [28]. (b) 3 dB bandwidth and gain–bandwidth product (GBP) reach 0.7 and 11 GHz at 65 V, respectively. The capacitance of the device limits the bandwidth since the bandwidth decreases with increasing device area. (c) Measured gain, $M$, as a function of reverse bias at three different temperatures: 296, 333, and 353 K. (d) $C_{bd}$ versus total depletion width for APDs of various materials: InP [23], Si [24], AlInAs [23], AlAsSb [25,29], and AlGaAsSb [10,30].

indicates that the bandwidth is limited by the RC time constant of the devices, not by the transit time.

One of the crucial performance metrics in APDs is the temperature coefficient of breakdown ($C_{bd}$), defined as the change in the breakdown voltage with temperature. In general, the breakdown voltage of an APD increases with increasing the temperature due to the increased phonon scattering reducing the ionization coefficients. This can significantly alter the multiplication (or gain) and hence sensitivity as the temperature changes in APDs made of materials such as InP [23] and Si [24]. To determine the $C_{bd}$ of our device, $M$ at various temperatures, 296 (23°C), 333 (60°C), and 353 K (80°C) were measured as shown in Fig. 4(c). The change in voltage with temperature at $M = 20$ was used rather than at breakdown, as this should give similar results without the risk of catastrophic damage to the devices. The device junction temperatures were accurately measured using the method described in Ref. [25], and the measured $C_{bd}$ was $\sim 11.8$ mV/K, which is $\sim 10\times$ lower than the Hamamatsu device ($C_{bd} = 100$ mV/K) [5]. Figure 4(d) compares $C_{bd}$ for this SACM APD and several other APD technologies as a function of total depletion thickness. The AlGaAsSb SACM APDs present significantly lower $C_{bd}$ than InP-, AlInAs-, and Si-based APDs and are comparable to results reported for AlAsSb- [25], AlGaAsSb- [10], and AlInAsSb- [26] based APDs. Ong *et al*. [27] showed that the alloy disorder potential was responsible for the large differences seen in the $C_{bd}$ of different semiconductors, and Monte Carlo modeling by Jin *et al*. [25] showed that increased alloy scattering relative to the phonon scattering in Sb-based alloys reduces the temperature dependence of the ionization coefficients, resulting in a much smaller $C_{bd}$. This suggests that these SACM APDs will not require significant temperature stabilization, potentially eliminating the need for a cooling subsystem.

## 4. DISCUSSION AND CONCLUSION

Recently, extremely low excess noise (and large $\alpha/\beta$ ratio) has been demonstrated with various As/Sb mixed alloys on InP substrates, such as AlGaAsSb [6,7], AlAsSb [31], and AlInAsSb [32]. As shown in Fig. 5(a), their noise values (pink ellipse) are significantly smaller than those of $P$- and As-bearing materials (blue ellipse). This observation, combined with the observed sub-McIntyre behavior, suggests that the ionization behavior of large group $V$ atom APDs (Sb) seem to be different compared to those of smaller group $V$ species ($P$ and As). Adding large Bi atoms into GaAs mainly engineers the valence band structure [33] and so, increases the spin–orbit splitting energy ($\Delta$so). Oguzman *et al*. [34] showed that in GaAs, the hole ionization process was largely initiated from the split-off band. Increasing $\Delta$so makes the transfer of holes from the heavy and light hole bands into the split-off band more difficult and hence reduces the hole impact ionization as shown in the GaAsBi system [35]. To investigate the effect of $\Delta$so on the $\alpha/\beta$ ratio for various material systems, we plot the calculated $\alpha/\beta$ ratio (at electric fields corresponding to $M = 1.1$ in 1 μm $p^+-i-n^+$ diodes) as a function of $\Delta$so, as shown in Fig. 5(b). It is clear that the $\alpha/\beta$ ratio increases with increasing $\Delta$so, and this correlates with the increasing size of the group V species in the alloys (N → P → As → As/Sb → As/Bi). With only 5.4% incorporation of Bi, $\Delta$so can reach up to ~0.6 eV and result in a $\alpha/\beta$ ratio that is even larger than $Al_{0.85}GaAsSb$. The ionization coefficients of InP, InAlAs, and AlAsSb show that the electric field dependence of $\alpha$ is identical in all three materials, but it is $\beta$ that decreases as $\Delta$so increases [36]. Similar behavior is seen in the GaAsBi material system with $\alpha$ changing only very slightly with increasing Bi but $\beta$ decreasing dramatically [33]. These findings suggest a means by which to engineer the valence band structure in bulk semiconductors and hence obtain deterministic gain.

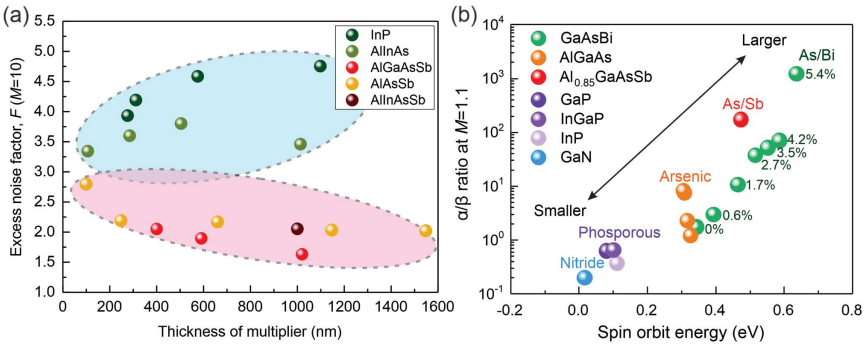


**Fig. 5.** (a) $F$ at $M = 10$ as a function of multiplier thickness for various material systems on InP substrates: AlGaAsSb (this work), InP [4], InAlAs [37], AlAsSb [31,38], and AlInAsSb [32]. The blue ellipse contains materials without Sb, while the pink ellipse contains Sb bearing materials. (b) $\alpha/\beta$ ratio at $M = 1.1$ versus spin–orbit energy for various material systems: GaN [39,40], GaP [41,42], InGaP [43,44], InP [25,45], $Al_xGa_{1-x}As$ [46–48], and $GaAs_{1-x}Bi_x$ [35]. The spin–orbit energy of $Al_{0.85}GaAsSb$ was theoretically calculated using a 14-band $k\cdot p$ method in this work.

Table 1 compares our non-optimized GaAsSb/AlGaAsSb SACM APD to three commercially available, 200 μm diameter InGaAs APDs to benchmark the performance of our device. The Hamamatsu G14858-0020AA is a low dark current design that was recently released [5]. The 200 μm GaAsSb/AlGaAsSb SACM APD (this work) is capable of an $M$ that is ∼ 10× higher, an $F$ (at $M = 25$) that is 6.5× lower, $C_{bd}$ that is ∼10× lower, and a similar bandwidth. However, the QE of the SACM APD (21.35%) at the unity gain point is less than that of this Hamamatsu APD (∼65%), which can be attributed to the thin GaAsSb absorber (460 nm) used here and lack of any AR coating. Therefore, the only performance limiting factor for the reported device is the bulk dark current from the GaAsSb absorption region, which is 24× higher, but even this compares favorably with the Hamamatsu G8931-20 variant. Comparison with the Excelitas APD is complicated by the fact that its dark current and $F$ are provided only at $M = 10$, but on most metrics, GaAsSb/AlGaAsSb compares favorably. Further optimization of the GaAsSb growth to reduce the dark currents to levels seen in InGaAs together with the use of an AR coating and a 2 μm thick GaAsSb absorber will improve the performance of this SACM APD significantly. This would increase the QE at unity gain to 87% giving potentially a maximum multiplied QE of 24,186%. The capacitance is also expected to be almost half, and this should lead to a doubling of the RC-limited device bandwidth to 1.4 GHz. $C_{bd}$ will also double if the total depletion width doubles, but at <24 mV/K, it is still > 4× better than these commercial InGaAs APDs.

In summary, this demonstration of an RT, high gain, and extremely low excess noise GaAsSb/AlGaAsSb SACM APD on InP shows improved sensitivity over Si and state-of-the-art commercial APDs for 1550 nm detection. The SACM APD growth and design can be improved to reduce the bulk dark currents, increase the multiplied QE with low excess noise, and extend the bandwidth from this initial demonstration. These characteristics will provide significant performance enhancements in lidar systems and other applications that require high sensitivity and fast response time APDs.

## 5. METHODS

### A. Material Growth

A total of five $p^+-i-n^+$ samples and one SACM sample were grown on semi-insulating InP substrates using a random alloy (RA) growth technique in a solid-state MBE reactor. All the materials were grown as RAs. For group V cells, we used RIBER VAC 500 and Veeco Mark V valved crackers for As and Sb, respectively. To achieve very low background doping concentration for both $p^+-i-n^+$ GaAsSb and AlGaAsSb, calibration runs were performed at various growth conditions such as growth rate, V/III beam equivalent pressure (BEP) ratio, and growth temperature. More details on the growth can be found elsewhere [6,7].

**Table 1. Comparison of This Work with a Commercial, State-of-the-Art Device by Hamamatsu[a]**

| Parameters | Excelitas (C30662) | Hamamatsu (G8931-20) | Hamamatsu (G14858-0020AA) | This Work (GaAsSb/AlGaAsSb) |
|---|---|---|---|---|
| Device diameter | 200 μm | 200 μm | 200 μm | 200 μm |
| Spectral range | ∼1.7 μm | ∼1.7 μm | ∼1.7 μm | ∼1.7 μm |
| Capacitance at max depletion | 2.5 pF | 1.5 pF | 2 pF | 2 pF |
| Breakdown voltage | 50 V | 55 V | 65 V | 70 V |
| $C_{bd}$ | 140 mV/K | 110 mV/K | 100 mV/K | 11.83 mV/K |
| Bandwidth | 0.85 GHz | 0.9 GHz | 0.9 GHz | 0.7 GHz |
| Max multiplication | ∼20 | ∼30 | ∼30 | ∼278 |
| Excess noise at $M = 25$ | 3.4 at $M = 10$ | ∼13 | ∼13 | ∼2 |
| Dark current at $M = 25$ | 4.5 nA at $M = 10$ | 2280 nA | 20 nA | 480 nA |

[a]While the device in our work has significantly greater gain and lower noise, further work is needed to reduce its dark current.

### B. Device Fabrication

Optimizing the device fabrication process is important to achieve high gain and low noise SACM APDs. If the fabrication is not done well, high leakage current and early edge breakdown prevent characterization of representative gain and noise of the APDs. For us to successfully perform the characterizations, iterative fabrication runs were carried out with characterization of current and noise characteristics to guide the optimization. The fabrication for the SACM APDs was done with conventional lithography and wet etching processes to delineate a clear mesa shape of the devices, and the surface was covered by SU-8 for passivation. Last, Ti/Au were deposited on the top and bottom contact layers to make ohmic contacts. The low series resistance for all devices was confirmed by forward IV characteristics. More details on the fabrication can be found elsewhere [6,7].

### C. IV and CV Measurements

The dark current–voltage measurements were performed with an HP4140B picoammeter and a probe station. CV measurements were undertaken using an HP4275A LCR meter as a frequency of 100 KHz. The depletion width and background doping concentration were determined with a static dielectric constant of 11.4 for AlGaAsSb and 14.1 for GaAsSb.

### D. Multiplication and Excess Noise

A transimpedance-amplifier-based circuit with a center frequency of 10 MHz and bandwidth of 4.2 MHz was used to determine the multiplication and excess noise in these structures as described in Ref. [49]. Phase-sensitive detection was used to remove the effects of the DC dark leakage current. The measurement setup was calibrated by using a reference device (SFH2701 Silicon PIN photodiode) that operates with shot noise only. The measured noise power of the device under test (DUT) was compared to the measured noise power of the reference device at a given photocurrent to determine the excess noise factor. A Thorlabs fiber-coupled LED (M1450F1) with an emission peak at 1550 nm was used to illuminate the devices for multiplication and excess noise measurements. The gain value of the GaAsSb/AlGaAsSb SACM at a given voltage was determined by comparing the absolute photocurrent value to a GaAsSb $p^+-i-n^+$ diode of identical optical sensing area at unity gain, correcting for differences in photon absorption.

### E. Quantum Efficiency

QE measurements are performed to study the optical properties of the SACM. A 100 W tungsten bulb source was focused into a monochromator (IHR320). The output light from the monochromator was focused onto the DUT using optical lenses. The light was modulated at 180 Hz by a mechanical chopper to remove any DC dark leakage current, and photocurrent was measured using a lock-in amplifier. The DUT was biased with a Keithley 236 source meter unit. A Thorlabs InGaAs photodiode (FD05D), with known responsivity, was used as a reference sample to calculate the relative power of the monochromator at each wavelength.

### F. Bandwidth Measurements

A CW optical signal from a 1.55 μm semiconductor laser was passed through a polarization controller and then modulated by a LiNbO3 MZM. A bias was applied to the modulator at the quadrature point, and it was driven by a VNA. Then, the modulated optical signal was focused onto the SACM device via a lensed fiber, and a G-S probe collected the photo-response. The VNA using a bias-tee measured the RF photo-response. More details can be found in Ref. [28].

**Funding.** Directed Energy-Joint Technology Office (N00014-17-1-2440); Engineering and Physical Sciences Research Council (EP/R513313/1).

**Acknowledgment.** The work of Harry Lewis was supported in part by an EPSRC studentship. S.L. and H.J. designed the structures and performed material growth, fabrication, and preliminary device characterizations for all GaAsSb PINs, AlGaAsSb PINs, and SACM structures. X.J. and H.L. undertook IV, CV, QE, multiplication, and excess noise for AlGaAsSb PINs and the SACM structure. Y.L. carried out the IV, CV, and QE on GaAsSb PINs. B.G. was responsible for bandwidth measurement on the SACM structure. C.H.G. calculated spin–orbit energy of AlGaAsSb using the 14-band $k \cdot p$ method. All authors discussed and analyzed the results, and S.L., X.J., H.J., B.G., C.H.G., J.C.C., J.P.R.D., and S.K. wrote the manuscript. S.K. helped with the design and data analysis and supervised the entire project. All authors reviewed and approved the manuscript.

**Disclosures.** The authors declare no conflicts of interest.

**Data availability.** The data that support the plots within this paper and other findings of this study are available from the corresponding author upon reasonable request.

**Supplemental document.** See Supplement 1 for supporting content.

†These authors contributed equally to this paper.

## REFERENCES

1. U. N. Singh, T. F. Refaat, S. Ismail, K. J. Davis, S. R. Kawa, R. T. Menzies, and M. Petros, "Feasibility study of a space-based high pulse energy 2 μm CO2 IPDA lidars," Appl. Opt. **56**, 6531–6547 (2017).
2. P. F. McManamon, *Lidar Technologies and Systems* (SPIE, 2019).
3. R. McIntyre, "Multiplication noise in uniform avalanche diodes," IEEE Trans. Electron Devices **ED-13**, 164–168 (1966).
4. P. Yuan, C. C. Hansing, K. A. Anselm, C. V. Lenox, H. Nie, A. L. Holmes, Jr., B. G. Streetman, and J. C. Campbell, "Impact ionization characteristics of III-V semiconductors for a wide range of multiplication region thicknesses," IEEE J. Quantum Electron. **36**, 198–204 (2000).
5. "Hamamatsu product datasheet: InGaAs APD (G14858-0020AA)," 2019, https://www.hamamatsu.com/content/dam/hamamatsu-photonics/sites/documents/99_SALES_LIBRARY/ssd/g14858-0020aa_kapd1068e.pdf.
6. S. Lee, S. H. Kodati, B. Guo, A. H. Jones, M. Schwartz, M. Winslow, C. H. Grein, T. J. Ronningen, J. C. Campbell, and S. Krishna, "Low noise Al0.85Ga0.15As0.56Sb0.44 avalanche photodiodes on InP substrates," Appl. Phys. Lett. **118**, 081106 (2021).
7. S. Lee, B. Guo, S. H. Kodati, H. Jung, M. Schwartz, A. H. Jones, M. Winslow, C. H. Grein, T. J. Ronningen, J. C. Campbell, and S. Krishna, "Random alloy thick AlGaAsSb avalanche photodiodes on InP substrates," Appl. Phys. Lett. **120**, 071101 (2022).
8. M. S. Park and J. H. Jang, "GaAs0.5Sb0.5 lattice matched to InP for 1.55 μm photo-detection," Electron. Lett. **44**, 549 (2008).
9. H. Inada, K. Miura, H. Mori, Y. Nagai, Y. Iguchi, and Y. Kawamura, "Uncooled SWIR InGaAs/GaAsSb type-II quantum well focal plane array," Proc. SPIE **7660**, 76603N (2010).
10. Y. Cao, T. Osman, E. Clarke, P. K. Patil, J. S. Ng, and C. H. Tan, "A GaAsSb/AlGaAsSb avalanche photodiode with a very small temperature coefficient of breakdown voltage," J. Lightwave Technol. **40**, 4709–4713 (2022).
11. Y. Xiao, Z. Li, and Z. S. Li, "Modeling of InGaAs/AlGaAsSb APDs with high gain-bandwidth product," Proc. SPIE **11498**, 114980R (2020).
12. S. Xie, X. Zhou, S. Zhang, D. J. Thomson, X. Chen, G. T. Reed, J. S. Ng, and C. H. Tan, "InGaAs/AlGaAsSb avalanche photodiode with high gain-bandwidth product," Opt. Express **24**, 24242–24247 (2016).
13. D. Hahn, O. Jaschinski, H.-H. Wehmann, A. Schlachetzki, and M. V. Ortenberg, "Electron-concentration dependence of absorption and

refraction in n-$In_{0.53}Ga_{0.47}As$ near the band-edge," J. Electron. Mater. **24**, 1357–1361 (1995).
14. I. Vurgaftman and J. R. Meyer, "Band parameters for III–V compound semiconductors and their alloys," J. Appl. Phys. **89**, 5815–5875 (2001).
15. P. Delvin, H. M. Heravi, and J. C. Woolley, "Electron effective mass values in $GaA_{sx}Sb_{1-x}$ alloys," Can. J. Phys. **59**, 939–944 (1981).
16. B. Guo, X. Jin, S. Lee, S. Z. Ahmed, A. H. Jones, X. Xue, B. Liang, H. I. J. Lewis, S. H. Kodati, D. Chen, T. J. Ronningen, C. H. Grein, A. W. Ghosh, S. Krishna, J. P. R. David, and J. C. Campbell, "Impact ionization coefficients of digital alloy and random alloy Al0.85Ga0.15As0.56Sb0.44 in a wide electric field range," J. Lightwave Technol. **40**, 4758–4764 (2022).
17. D. S. Ong, A. H. Tan, K. Y. Choo, K. H. Yeoh, and J. P. R. David, "Weibull-Fréchet random path length model for avalanche gain and noise in photodiodes," J. Phys. D **55**, 065105 (2021).
18. "Hamamatsu product datasheet: Si APD (S10341 series)," 2017, https://www.hamamatsu.com/resources/pdf/ssd/s10341_series_kapd1030e.pdf.
19. D. S. Ong, K. F. Li, G. J. Rees, J. P. R. David, and P. N. Robson, "A simple model to determine multiplication and noise in avalanche photodiodes," J. Appl. Phys. **83**, 3426–3428 (1998).
20. M. J. Sun, K. H. Nichols, W. S. C. Chang, R. O. Gregory, F. J. Rosenbaum, and C. M. Wolfe, "Gallium arsenide electroabsorption avalanche photodiode waveguide detectors," Appl. Opt. **17**, 1568–1578 (1978).
21. T. E. V. Eck, L. M. Walpita, W. S. C. Chang, and H. H. Wieder, "Franz–Keldysh electrorefraction and electroabsorption in bulk InP and GaAs," Appl. Phys. Lett. **48**, 451–453 (1986).
22. W. Weng, J. Larsson, J. Bood, M. Alden, and Z. Li, "Quantitative hydrogen chloride detection in combustion environments using tunable diode laser absorption spectroscopy with comprehensive investigation of hot water interference," Appl. Spectrosc. **76**, 207–215 (2022).
23. L. J. J. Tan, D. S. G. Ong, J. S. Ng, C. H. Tan, S. K. Jones, Y. Qian, and J. P. R. David, "Temperature dependence of avalanche breakdown in InP and InAlAs," IEEE J. Quantum Electron. **46**, 1153–1157 (2010).
24. D. J. Massey, J. P. R. David, and G. J. Rees, "Temperature dependence of impact ionization in submicrometer silicon devices," IEEE Trans. Electron Devices **53**, 2328–2334 (2006).
25. X. Jin, S. Xie, B. Liang, X. Yi, H. Lewis, L. W. Lim, Y. Liu, B. K. Ng, D. L. Huffaker, C. H. Tan, D. S. Ong, and J. P. R. David, "Temperature dependence of the impact ionization coefficients in AlAsSb lattice matched to InP," IEEE J. Sel. Top. Quantum Electron. **28**, 3801208 (2021).
26. A. H. Jones, S. D. March, S. R. Bank, and J. C. Campbell, "Low-noise high-temperature AlInAsSb/GaSb avalanche photodiodes for 2-μm applications," Nat. Photonics **14**, 559–563 (2020).
27. J. S. L. Ong, J. S. Ng, A. B. Krysa, and J. P. R. David, "Temperature dependence of avalanche multiplication and breakdown voltage in Al0.52In0.48P," J. Appl. Phys. **115**, 064507 (2014).
28. D. Chen, K. Sun, Y. Shen, A. H. Jones, A. A. Dadey, B. Guo, J. A. McArthur, S. R. Bank, and J. C. Campbell, "Frequency behavior of AlInAsSb nBn photodetectors and the development of an equivalent circuit model," Opt. Express **30**, 25262–25276 (2022).
29. S. Xie and C. H. Tan, "AlAsSb avalanche photodiodes with a sub-mV/K temperature coefficient of breakdown voltage," IEEE J. Quantum Electron. **47**, 1391–1395 (2011).
30. B. Guo, S. Z. Ahmed, X. Xue, A.-K. Rockwell, J. Ha, S. Lee, B. Liang, A. H. Jones, J. A. McArthur, S. H. Kodati, T. J. Ronningen, S. Krishna, J. S. Kim, S. R. Bank, A. W. Ghosh, and J. C. Campbell, "Temperature dependence of avalanche breakdown of AlGaAsSb and AlInAsSb avalanche photodiodes," J. Lightwave Technol. **40**, 5934–5942 (2022).
31. X. Yi, S. Xie, B. Liang, L. W. Lim, J. S. Cheong, M. C. Debnath, D. L. Huffaker, C. H. Tan, and J. P. R. David, "Extremely low excess noise and high sensitivity AlAs0.56Sb0.44 avalanche photodiodes," Nat. Photonics **13**, 683–686 (2019).
32. S. H. Kodati, S. Lee, B. Guo, A. H. Jones, M. Schwartz, M. Winslow, N. A. Pfiester, C. H. Grein, T. J. Ronningen, J. C. Campbell, and S. Krishna, "AlInAsSb avalanche photodiodes on InP substrates," Appl. Phys. Lett. **118**, 091101 (2021).
33. K. Alberi, O. D. Dubon, W. Walukiewicz, K. M. Yu, K. Bertulis, and A. Krotkus, "Valence band anticrossing in $GaBi_xAs_{1-x}$," Appl. Phys. Lett. **91**, 051909 (2007).
34. I. H. Oğuzman, Y. Wang, J. Kolník, and K. F. Brennan, "Theoretical study of hole initiated impact ionization in bulk silicon and GaAs using a wave-vector-dependent numerical transition rate formulation within an ensemble Monte Carlo calculation," J. Appl. Phys. **77**, 225–232 (1995).
35. Y. Liu, X. Yi, N. J. Bailey, Z. Zhou, T. B. O. Rockett, L. W. Lim, C. H. Tan, R. D. Richards, and J. P. R. David, "Valence band engineering of GaAsBi for low noise avalanche photodiodes," Nat. Commun. **12**, 1–8 (2021).
36. X. Yi, S. Xie, B. Liang, L. W. Lim, X. Zhou, M. C. Debnath, D. L. Huffaker, C. H. Tan, and J. P. R. David, "Demonstration of large ionization coefficient ratio in AlAs0.56Sb0.44 lattice matched to InP," Sci. Rep. **8**, 9107 (2018).
37. Y. L. Goh, A. R. J. Marshall, D. J. Massey, J. S. Ng, C. H. Tan, M. Hopkinson, J. P. R. David, S. K. Jones, C. C. Button, and S. M. Pinches, "Excess avalanche noise in $In_{0.52}Al_{0.48}As$," IEEE J. Quantum Electron. **43**, 503–507 (2007).
38. J. Xie, S. Xie, R. C. Tozer, and C. H. Tan, "Excess noise characteristics of thin AlAsSb APDs," IEEE Trans. Electron Devices **59**, 1475–1479 (2012).
39. L. Cao, J. Wang, G. Harden, H. Ye, R. Stillwell, A. J. Hoffman, and P. Fay, "Experimental characterization of impact ionization coefficients for electrons and holes in GaN grown on bulk GaN substrates," Appl. Phys. Lett. **112**, 262103 (2018).
40. A. Wolos, Z. Wilamowski, C. Skierbiszewski, A. Drabinska, B. Lucznik, I. Grzegory, and S. Porowski, "Electron spin resonance and Rashba field in GaN-based materials," Physica B **406**, 2548–2554 (2011).
41. R. A. Logan and A. G. Chynoweth, "Charge multiplication in GaP p-n junctions," J. Appl. Phys. **33**, 1649–1654 (1962).
42. S. E. Stokowski and D. D. Sell, "Reflectivity and (dR/dE)/R of GaP between 2.5 and 6.0 eV," Phys. Rev. B. **5**, 1636 (1972).
43. C. H. Tan, R. Ghin, J. P. R. David, G. J. Rees, and M. Hopkinson, "The effect of dead space on gain and excess noise in $In_{0.48}Ga_{0.52}P$ p+in+ diodes," Semicond. Sci. Technol. **18**, 803 (2003).
44. R. G. Alonso, A. Mascarenhas, S. Froyen, G. S. Horner, K. Bertness, and J. M. Olson, "Polarized piezomodulated reflectance study of spontaneous ordering in GaInP2," Solid State Commun. **85**, 1021–1024 (1993).
45. J. Peretti, H.-J. Drouhin, D. Paget, and A. Mircéa, "Band structure of indium phosphide from near-band-gap photoemission," Phys. Rev. B **44**, 7999 (1991).
46. M. Levinshtein, *Handbook Series on Semiconductor Parameters* (World Scientific, 1997), Vol. **1**.
47. S. A. Plimmer, J. P. R. David, G. J. Rees, and P. N. Robson, "Ionization coefficients in $Al_xGa_{1-x}As$ (x = 0-0.60)," Semicond. Sci. Technol. **15**, 692 (2000).
48. B. K. Ng, J. P. R. David, S. A. Plimmer, G. J. Rees, R. C. Tozer, M. Hopkinson, and G. Hill, "Avalanche multiplication characteristics of Al0.8Ga0.2As diodes," IEEE Trans. Electron Devices **48**, 2198–2204 (2001).
49. K. S. Lau, C. H. Tan, B. K. Ng, K. F. Li, R. C. Tozer, J. P. R. David, and G. J. Rees, "Excess noise measurement in avalanche photodiodes using a transimpedance amplifier front-end," Meas. Sci. Technol. **17**, 1941 (2006).